Incommensurate charge density wave order in U_2Ti

Callum R. Stevens,* Andreas Hermann, and Andrew Huxley
School of Physics and Astronomy and CSEC, University of Edinburgh, Edinburgh EH9 3FD, United Kingdom

Didier Wermeille
XMaS Beamline, European Synchrotron Radiation Facility, 71 Avenue des Martyrs, Grenoble 38043, France

(Received 21 September 2023; revised 10 January 2024; accepted 7 February 2024; published 11 March 2024)

Density functional theory predicted that the ground state of U_2Ti should undergo a Peierls-like doubling of its unit cell along the c axis on cooling from high temperature [G. Kaur *et al.*, J. Alloys Compd. **730**, 36 (2018)]. We report x-ray diffraction, heat capacity, and resistivity measurements showing that with decreasing temperature the transition from the parent hexagonal structure occurs in two steps, via an incommensurate state below $T_{ICDW} = 71(1)$ K which then undergoes a lock-in transition to the predicted commensurate Peierls-like state at $T_{CCDW} = 46(3)$ K. The signatures of the upper transition in thermodynamic and transport measurements are weak, meaning that similar incommensurate charge density waves (ICDWs) preceding CDWs might occur more widely in other systems but elude detection. The collinear nature of both the ICDW and Peierls-like states we report is much simpler than more complex incommensurate states seen in α-U, which may in time provide greater insight into the mechanism for ICDW formation.

DOI: 10.1103/PhysRevB.109.125116

I. INTRODUCTION

Slow charge fluctuations, linked to nearby charge density waves (CDWs) may play an important role in the formation of strange-metal states in high-temperature superconductors [1,2] and heavy fermions [3,4]. This motivates the need for a better understanding of the CDW order itself and its interplay with both magnetism and superconductivity.

Most CDWs are found in strongly one- or two-dimensional materials, including the high-temperature superconductors (SCs) [5], transition metal tri- and dichalcogenides [6], and the linear chain organic conductors [7]. In some of these materials CDW order coexists with SC but in others only one order is present at a time as an external parameter such as pressure is varied. Where CDW and SC occur simultaneously, they may still compete as in $2H$-$NbSe_2$ [8]. Recent observations of geometrically frustrated 2D systems, such as FeGe [9], show magnetic and charge interactions that are highly intertwined.

Clear examples of CDW order in three dimensions are much rarer. α-U is the outstanding example [10]. α-U has an orthorhombic crystal structure and multiple CDW transitions. The highest temperature state is incommensurate with the lattice in all three crystallographic directions, and subsequently undergoes lock-in transitions for different wave vector components in turn as the temperature is reduced. In the incommensurate states different symmetry related q vectors give rise to microscopic domains that complicate the interpretation of experiments; attempts to produce monodomain incommensurate charge density wave (ICDW) α-U crystals are ongoing [11].

Other materials with 3D CDW order include $LuPt_2In$ [12], $R_5Ir_4Si_{10}$ (R = Dy, Ho, Tm and Yb) [13], and $IrTe_2$ [14]. However, these systems are not known to show separate incommensurate/commensurate transitions. $Er_5Ir_4Si_{10}$ does display an ICDW/CCDW transition. Below 155 K, the CDW wave vector has a commensurate component $(0, 0, 1/2)$ and an incommensurate component $(0, 0, 1/4 - \delta)$ where δ drops sharply to zero at 55 K [15]. The existence of a commensurate component alongside the ICDW makes it difficult to quantify the contribution of each order to macroscopic properties.

A 3-dimensional material allowing the study of ICDWs, free from domain structure and free of magnetic order, is lacking. As we will show, hexagonal U_2Ti has a simple single-component ordering wave vector, while maintaining 3D metallicity, so potentially may provide such a material.

Density functional theory (DFT) calculations for the reported room temperature crystal structure of U_2Ti show an instability of a longitudinal optical phonon at $(0, 0, 1/2)$ [16]. The energy of the crystal structure is minimized by dimerization of uranium sites along the hexagonal c axis.

We report diffraction measurements consistent with this predicted low-temperature structure but further reveal an incommensurate phase between $T_{CCDW} = 46(3)$ K and $T_{ICDW} = 71(1)$ K. The heat capacity shows a weak shoulder feature at T_{ICDW} and a larger cusplike peak at T_{CCDW}. The temperature derivative of resistivity shows a sharp variation at the lower transition only.

*csteven7@exseed.ed.ac.uk

Kaur *et al.* [16] proposed that Fermi surface nesting may drive the formation of CDW order in U_2Ti. It is well established that Fermi surface nesting cannot by itself account for CDW formation except for 1-dimensional systems. Favorable electron-phonon coupling and off-Fermi-surface contributions also need to be considered [17]. Off-Fermi-surface contributions, sometimes called "hidden nesting," refer to a matching of the Fermi velocity (with opposite sign) at the surfaces linked by the CDW wave vector. As shown for α-U, unlike in the 1D Peierls mechanism, a critical magnitude of electron-phonon coupling is also required [18,19]. An alternative mechanism for CDW/spin density wave (SDW) order not requiring a critical degree of electron-phonon coupling or nesting was proposed by Overhauser [20] and is driven by exchange and correlation interactions. Such a theory has been applied to potassium [21,22]. However, the absence of CDW satellites in neutron diffraction means the presence of CDW order in potassium has not been unambiguously identified and Overhauser's mechanism has gained little traction more widely.

Most theoretical investigations of α-U largely focus on understanding the ordering vector at the coarse scale of the low-temperature commensurate order and do not address the small differences from this in the incommensurate states [19,23]. Phenomenologically, a Ginzburg-Landau (GL) analysis gives a good account of lock-in transitions in general [24]. The standard model starts with an incommensurate CDW instability and an undistorted unordered band structure. The CDW vector changes to become commensurate as the temperature is lowered and the amplitude of the order increases. The terms in the GL analysis that modify the modulation period are attributed to umklapp processes and harmonics of the primary order. A first-principles microscopic estimate of the magnitude of these terms is however lacking.

Quantum order by disorder (QOBD) affords a different explanation for incommensurate phases [25]. The QOBD theory was developed to explain incommensurate magnetic orders. For example, in the case of PrPtAl there is an incommensurate SDW above a lower temperature transition to ferromagnetic order [26]. The key concept is that the Fermi surface distortion for an ICDW enhances the phase space available for low-energy fluctuations more than a CCDW. The nesting vector could then be commensurate, but the resulting order is driven to be incommensurate by QOBD. As temperature is lowered and the role of excitations reduces, the primary commensurate order asserts itself. This mechanism is distinguished from the model described in the previous paragraph in having a primary order that is commensurate in the absence of fluctuations rather than incommensurate.

Studying simpler systems than α-U, such as U_2Ti, will help distinguish between these different mechanisms to better understand the origin of ICDWs.

The paper is organized as follows. In Sec. II preparation of twinned crystal samples of U_2Ti and the experimental methods are discussed. Section III discusses DFT calculations of the electronic susceptibility to quantify the predicted ordering vector for U_2Ti. Section IV discusses the experimental results supporting the identification of a commensurate to incommensurate CDW transition. Finally, Sec. V summarizes the main findings and conclusions.

II. EXPERIMENTAL DETAILS

A. Synthesis

Samples of U_2Ti were prepared by melting depleted U (Ames Laboratory, electrotransported, >99.99%) and Ti (Goodfellow, >99.999% purity) in a radio frequency induction furnace under ultrahigh vacuum. The melt was sustained at a temperature between 1415–1460 K for at least 1.5 h, while levitated above a water-cooled oxygen-free high-conductivity copper crucible. The melt is quenched at several 100 °C s^{-1} by abruptly cutting the radio frequency field. Sections of the quenched melt were spark cut for annealing. All sections were annealed at a temperature between 950–1000 K for at least 5 days, cooling to room temperature at a rate slower than 22 °C h^{-1}. This produced twinned hexagonal U_2Ti crystals from the high-temperature disordered cubic phase. Twinned regions have their c axes orientated along the four possible diagonals of a cube ([1,1,1] directions). Twinned crystalline samples of U_2Ti were spark cut from the annealed sections. The twin boundaries are separated by ∼100 μm.

The sample used for resistivity measurements underwent an additional low-temperature anneal. The sample was wrapped in Ta foil and placed in an evacuated quartz tube placed in a tube furnace at 830(5) °C for 15 days. The residual resistivity ratio, RRR, improved moderately from 2.8 to 3.7. Other annealed samples had RRRs in the range 1.7–7.8 and displayed similar features in their resistivity and heat capacity.

B. X-ray diffraction

X-ray diffraction (XRD) was performed on a polished twinned sample mounted on a Huber 6-circle diffractometer at the XMaS beamline, ESRF [27]. A wavelength of (0.8266 ± 0.0001) Å was used. The energy full width at half maximum (FWHM) of the beam is $\Delta E/E = 1.7 \times 10^{-4}$ at 10 keV and is the same magnitude at 15 keV. The beam size (FWHM) at the sample is ∼70 μm vertically and ∼60 μm horizontally.

To mitigate the variation of diffraction intensity due to sample texture/roughness and beam translation, the beam position on the sample was optimized to give the greatest diffraction intensity for each reflection measured. At each temperature the starting position was set to the optimized base temperature position and x, y, and x scans (40 uniform steps over ±100 μm) made to recenter on the position of maximum intensity. The integrated intensity was numerically integrated from rocking curve scans of reflections at $(1, 0, 3 + q_c)$, $(2, 0, 3 + q_c)$, and $(2, 1, 3 + q_c)$, where q_c is the CDW wave vector. Rocking curves comprised 80 steps of $\Delta\theta = 0.025°$.

C. Heat capacity

The heat capacity of a 44.29 mg sample was measured with a commercial PPMS from 1.8 K to 300 K. Heater pulses were such that the sample temperature rose by ≈2.0% over one time constant. A two-time-constant model is used to extract heat capacity from the measured heating/cooling curves [28].

D. Resistivity

Resistivity of an unorientated sample was measured with a phase-sensitive four-probe method with an ac current at

77 Hz of root mean square amplitude 1.00 mA. Magnetic field was applied perpendicular to the current and the magnitude is accurate to within 0.1%. A Cernox thermometer was used to measure sample temperature. The measurement is not corrected for magnetoresistance of the thermometer, though at 4 K and a field of 9 T, the correction is $\lesssim$30 mK and this does not significantly affect interpretation of the measurements [29].

E. Hall coefficient

The Hall voltage of an unorientated sample was measured with a phase-sensitive four-probe method with an ac current at 30 Hz of root mean square amplitude 8.00 mA. The sample was polished to a thickness of 460(20) μm. A magnetic field of ±8 T was applied perpendicular to the current and the magnitude is accurate to within 0.1%. A Cernox thermometer was used to measure sample temperature.

The Hall coefficient is obtained from the field-antisymmetrized (±8 T) transverse resistance curves.

III. DENSITY FUNCTIONAL THEORY CALCULATIONS

A. Computational details

Electronic structure DFT calculations were performed with a plane-wave basis set as implemented in the VASP code [30]. The electron-ion interaction was modeled using projector augmented wave (PAW) data sets, with the U $6s^2 6p^6 7s^2 (5f6d)^4$ and Ti $3s^2 3p^6 (4s3d)^4$ electrons in the valence space. Electron-electron exchange-correlation effects were modeled using the Perdew-Burke-Ernzerhof (PBE) functional [31]. Electronic wave functions were expanded in plane waves up to a cut-off energy $E_c = 600$ eV, and Brillouin zone sampling used regular k-point grids with linear density $40/\text{Å}^{-1}$ for all total energy calculations ($120/\text{Å}^{-1}$ for DOS and Fermi surface calculations). Geometries were optimized until remaining force components were below 1 meV Å^{-1} and stress tensor components below 1 meV Å^{-3} (0.16 GPa). Phonon calculations used the finite-displacement method in (3,3,4) supercells of the room temperature crystal structure and were set up and analyzed with the PHONOPY code [32]. Spin-polarized calculations considered on-site repulsion terms for the U $5f$ states (rotationally invariant DFT+U method [33]) up to magnitude $U = 5$ eV.

B. DFT+U

The inclusion of a Hubbard on-site repulsion term U affects the calculated structural and electronic properties of U_2Ti. Generally, both a and c lattice constants increase with increasing U. For the room temperature structure, the best agreement with experimental data is at $U = 1$ eV, where the optimized lattice constants are $a = 4.821$ Å and $c = 2.841$ Å; for $U \geqslant 2$ eV, agreement is worse. The electronic structure at the Fermi level also changes substantially for $U \geqslant 2$ eV, and phonon calculations predict dynamical instabilities across much of the Brillouin zone. As this does not correspond to experimental findings, we conclude the electronic structure is better described with $U \leqslant 1$ eV. In addition, $U = 1$ eV predicts that the ground state of U_2Ti, in the doubled unit cell, is magnetic; the calculated moment is small, about 1.2 μ_B/cell. There is no indication of a magnetic ground state from experiments. This suggests a failure of DFT+U to describe the on-site electronic correlations in this compound, and a combination of DFT with dynamical mean field theory (DFT+DMFT [34]) might be more suitable to reproduce the energy spectrum of the electron quasiparticles that couple to lattice degrees of freedom [35,36], but is beyond the scope of this work. For standard PBE calculations ($U = 0$ eV) magnetism does not seem to be favorable; any enforcement of finite spin moment on the U-atom sites leads to an increase in energy. Therefore, we discuss standard PBE results from here on.

C. Structure and phonon dispersions

The spin-degenerate calculations reproduce the results by Kaur *et al.* [16]: the lattice constants of the room temperature structure, $a = 4.782$ Å and $c = 2.808$ Å, are in good agreement with experiment; phonon calculations reveal a dynamical instability at the A point, $q = (0, 0, 1/2)$, due to an imaginary LO phonon mode; the structure in the doubled unit cell, with U atoms displaced along the c axis, is energetically (∼34 meV/f.u.) and dynamically stable. The doubled unit cell sees U atoms displaced by about 0.15 Å, the a axis contracted by about 0.016 Å, and the c axis expanded by about 0.080 Å.

D. Fermi surface nesting and the Lindhard function

Figure 1 shows the Fermi surface (FS) of the room temperature U_2Ti structure at the DFT-optimized lattice constants. Four bands cross the Fermi energy. The FS sheets comprise localized pockets centered on the Γ and K points (band 1), centered on the A points (band 4), and centered on a point along the Γ-A line (band 3), plus corrugated sheets in the k_x-k_y plane with connecting tubes along the k_z direction (bands 2 and 3). The projection of the lm components corresponding to U $5f$ states onto the sheets from bands 2 and 3 is also plotted.

We now explore possible nesting of the two largest Fermi surface sheets. Kaur *et al.* suggested nesting within the sheet(s). Here, we quantify the nesting function by determining the band pair-resolved static dielectric susceptibility,

$$\chi_0^{ij}(\mathbf{q}) = -\sum_{\mathbf{k}} \frac{f_j(\mathbf{k}) - f_i(\mathbf{k}+\mathbf{q})}{\epsilon_j(\mathbf{k}) - \epsilon_i(\mathbf{k}+\mathbf{q}) + \imath\eta}, \tag{1}$$

where $f_i(\mathbf{k})$ is the Fermi-Dirac occupancy of band i at point $\mathbf{k}$ in the Brillouin zone, and $\epsilon_i(\mathbf{k})$ the band energy. For f_i, we use an electronic temperature of 20 K, and $\eta = 10^{-6}$ eV for the broadening. The exact choice for these parameters is not critical. The k-point grid for the summation is (29,29,43). The matrix element linking different states is taken to be band and q independent.

Figure 2(a) shows $\mathbb{R}\mathrm{e}\chi_0^{ij}(0, 0, q_z)$ as a function of q_z, for each pair of bands (i, j). The strongest contribution occurs for $q_z = 1/2$ (in units of the reciprocal lattice), for transitions between bands 2 and 3. The contribution $\chi_0^{23}(q_x, q_y, 0.5)$ in the perpendicular plane is shown in Fig. 2(b). The variation is almost flat with only a weak maximum at $(q_x, q_y) = (0, 0)$. We conclude that the nesting is strongest at exactly $(0, 0, 1/2)$ but only weakly peaked in the plane $\perp$ **c**.

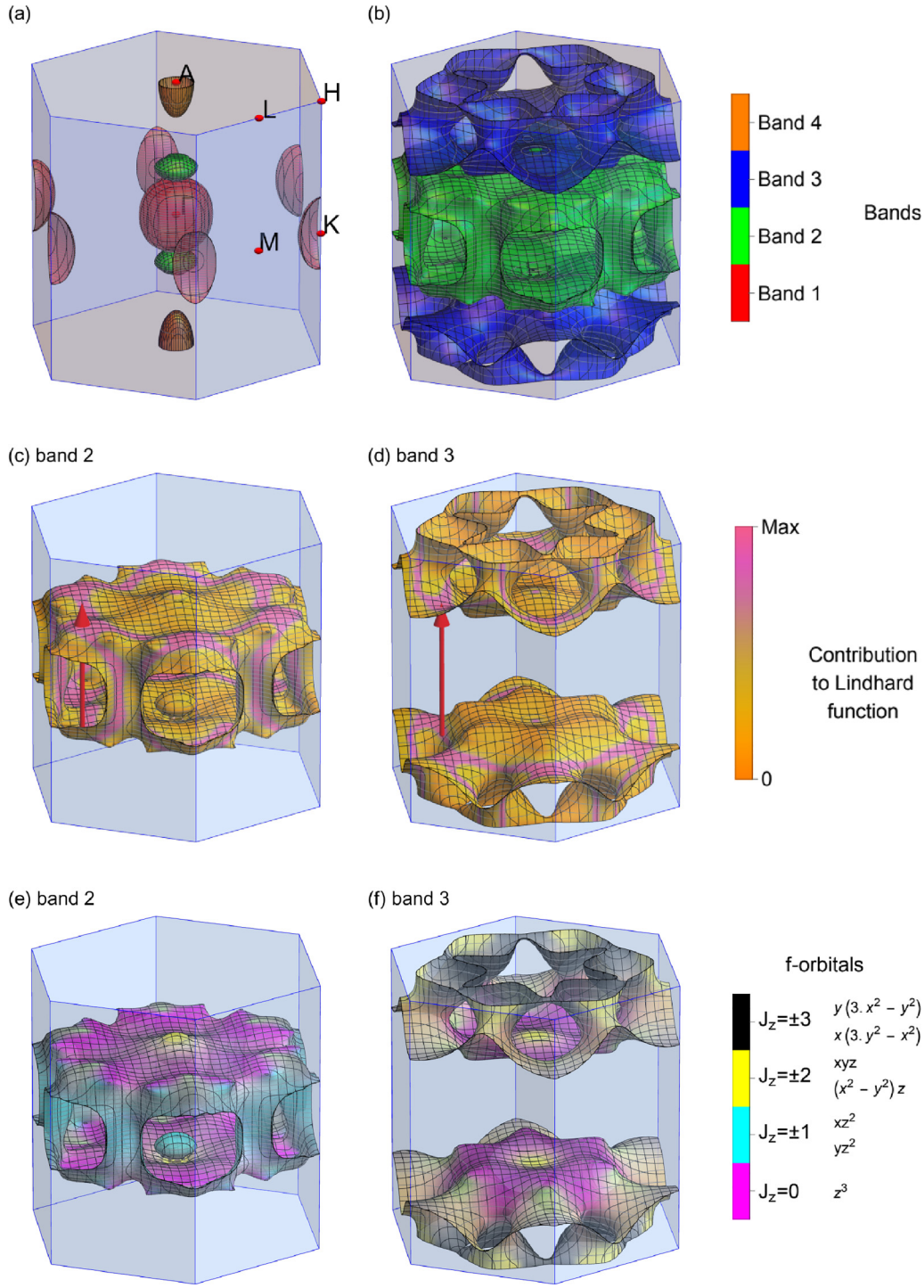

FIG. 1. Panels (a) and (b) show the different Fermi surface sheets. Band 1 (red) comprises electron pockets centered on Γ and K points. Band 2 (green) comprises two large sheets at approximately $(0, 0, \pm 0.25)$ linked by vertical tubes centered on M points [in panel (b)] and two small detached deformed ellipsoids, shown for clarity in panel (a). Band 3 (blue) comprises two sheets at $(0, 0, \pm 0.3)$ linked by inclined tubes. Band 4 (orange) comprises a single ellipsoidal surface centered on A. Panels (c) and (d) show the contribution to the Lindhard function with $q = (0, 0, 0.5)$ from transitions between bands 2 and 3. The color represents the contribution from the vicinity of each point on these Fermi surfaces. The pink regions represent regions making the largest contribution. The red arrow shows a vector (0,0,0.5) that links strongly contributing regions on the two sheets. Panels (e) and (f) show the f-orbital character of the Fermi surfaces on bands 2 and 3. The sheets can be crudely described as 2D sheets intersected by vertical tubes. The sheets have $J_z = 0$ (z^3) orbital character and the tubes $J_z = \pm 1$ (xz^2 and yz^2) character.

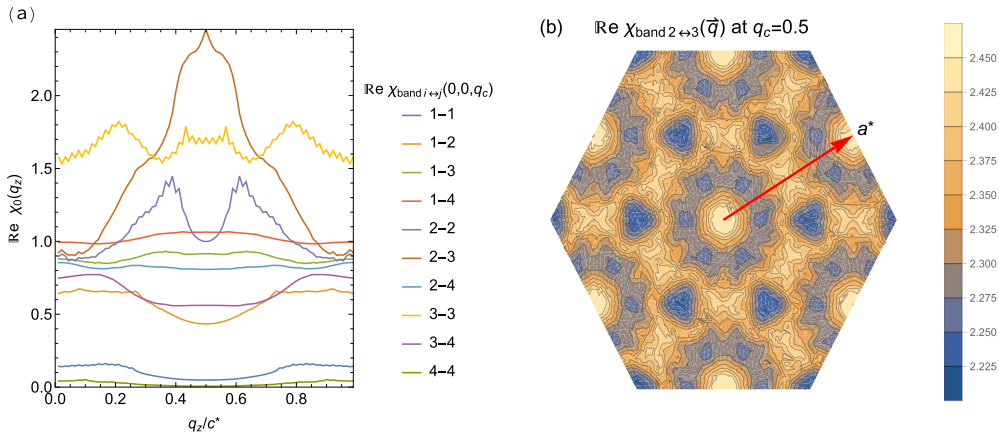

FIG. 2. Panel (a) compares the density of states factors in the calculation for the real part of the Lindhard function for momentum transfer $(0, 0, q_c)$ from different interband transitions. The largest contribution is at $q_c = 1/2$ for transitions between bands 2 and 3. Panel (b) shows the contribution to the real part of the Lindhard function for transitions between bands 2 and 3 for $q = (q_x, q_y, 1/2)$. The contribution is almost flat but weakly peaked at $(0, 0, 1/2)$.

Figures 1(c) and 1(d) show the contribution to $\mathbb{R}e\chi_0^{23}(0, 0, 1/2)$ from different parts of the Fermi surfaces of bands 2 and 3. The peak in the Lindhard function is seen to come from two regions: first, nesting running along a ring linking planar regions of the FS sheets of bands 2 and 3; second, from nesting between the tubes along k_z. The orbital projections in Figs. 1(e) and 1(f) show that the nesting involves orbitals with dominant $f_{z^2x,\,z^2y}$ character on band 2 and $f_{zxy,\,z(x^2-y^2)}$ character on band 3. While nesting of the planar regions alone might suggest that a simple 1D model could describe the formation of the CDW this overlooks equally important contributions from the tube nesting. The above analysis also ignores any q and band dependence of the matrix elements appearing in the Lindhard function.

IV. RESULTS AND DISCUSSION

A. Crystal structure

At room temperature U_2Ti has a hexagonal structure (known as the δ phase), space group $P6/mmm$, with $a = 4.828$ Å and $c = 2.847$ Å [37]. The nearest and next-nearest U-U spacings are 2.80 Å in the a-b plane and 2.85 Å along the c axis, compared with 2.74 Å and 2.84 Å for α-U, respectively. The δ phase forms below 898 °C [38] from the γ phase. The γ phase is body-centered cubic (space group $Im\bar{3}m$) with sites randomly occupied by U and Ti. The low-temperature distorted structure, predicted by Kaur *et al.* [16], is labeled δ_2.

Figure 3 shows projections of the different crystal structures of U_2Ti (see also Fig. 4 for a comparison of the structures of U_2Ti and α-U). The cubic γ phase distorts along a $[1, 1, 1]$ cubic direction to form the c axis of the δ-hexagonal unit cell. Since this direction is not unique the growth procedure described in Sec. II produced twinned samples. As discussed in Sec. IV B, below $T_{\text{ICDW}} = 71(1)$ K an incommensurate modulation at the uranium sites occurs along the c axis and below $T_{\text{CCDW}} = 46(3)$ K this modulation locks in to become periodic with the crystal lattice resulting in a doubling of the δ cell to give the δ_2 structure.

B. X-ray diffraction

The 10 K XRD pattern reveals additional reflections compared with room temperature at some $(h, k, l + q_c)$ positions, with $q_c = \frac{1}{2}$. The intensity and relative positions of these reflections compared to the lattice Bragg reflections were measured as a function of temperature. A weak reflection at $(1, 1, 4.5)$ has an integrated intensity $\sim \times 10^{-4}$ that of the $(1, 0, 3.5)$, $(2, 0, 3.5)$, and $(2, 1, 3.5)$ reflections, and has

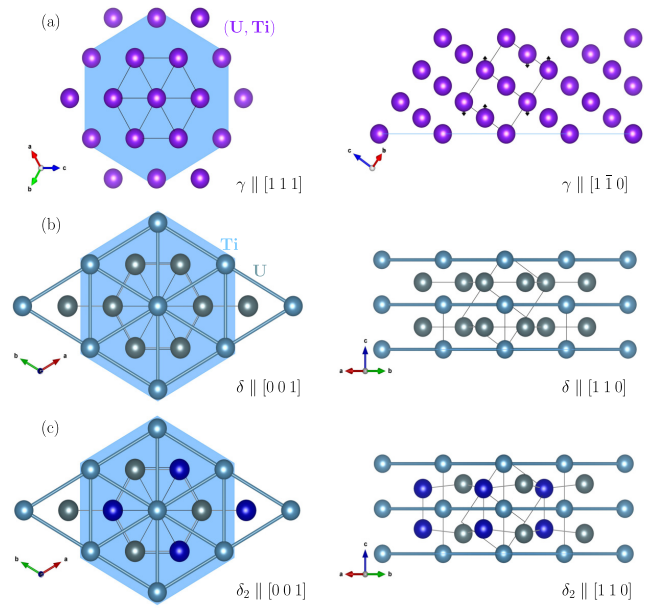

FIG. 3. Projections of the different crystalline structures of U_2Ti: (a) disordered cubic (γ) structure formed above 898 °C, (b) ordered hexagonal (δ) structure, (c) distorted (δ_2) structure predicted by Kaur *et al.* and formed below T_{CCDW}. The displacements of U sites has been enlarged for clarity. The original high-temperature cubic unit cell is shown by the black outline and a portion of the hexagonal $(0\,0\,1)$ plane is shown to highlight the projected sixfold symmetry. The black arrows on the γ phase indicate the direction of displacements of atoms which give rise to the δ phase.

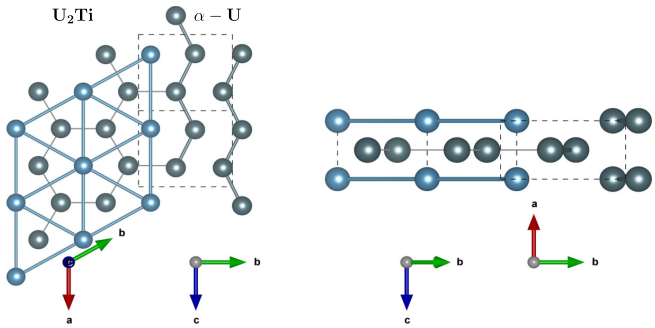

FIG. 4. Comparison of the U_2Ti and α-U structures. The left shows a view of U_2Ti along the hexagonal axis and an epitaxial alignment of uranium looking along the orthorhombic a axis. The right shows the perpendicular view. In U_2Ti the Peierls-like displacements are along the c direction and in α-U the predominant displacement is along the a direction.

a ratio of peak intensity to background of ≈1.5. Such a reflection may originate from multiple scattering or stacking faults in the hexagonal unit cell. Azimuthal scans were not performed to distinguish these two possibilities. No reflections occur at equivalent positions at $(1, 1, 3.5)$, $(0, 0, 3.5)$, and $(0, 0, 4.5)$. An overview of observed CDW reflections in diffraction space is shown in Fig. 5(a) with absent and weak reflections labeled. The allowed reflections lie on a honeycomb lattice in the h-k plane, consistent with the predicted structure of the low-temperature δ_2 state shown in Fig. 3.

Figure 5(b) shows the averaged normalized intensity, I_{CDW}, for the reflections $(1, 0, 3 + q_{\mathrm{CDW}})$, $(2, 0, 3 + q_{\mathrm{CDW}})$, and $(2, 1, 3 + q_{\mathrm{CDW}})$, and Fig. 5(c) the charge density wave ordering vector, q_{CDW}, determined from maximizing the intensity of the $(1, 0, 3 + q_{\mathrm{CDW}})$ and $(0, 1, 3 + q_{\mathrm{CDW}})$ reflections. Below T_{ICDW} an incommensurate CDW with a temperature-dependant q_{CDW} forms which then locks onto the commensurate value of $q_c \sim 0.5$ below $T_{\mathrm{CCDW}} = 46(3)$ K.

Below 40 K the data are well described by the BCS gap equation commonly used to describe CDWs. The fitted transition temperature is $T_{\mathrm{CCDW}} = 46(3)$ K in agreement with the transition identified in heat capacity measurements. For temperatures above 45 K the intensity has an approximately linear T dependence falling to zero at $T_{\mathrm{ICDW}} = 71(1)$ K.

If the ICDW state were to be confined to the surface it would be challenging to explain why q_{CDW} evolved smoothly to the bulk value at T_{CCDW} with decreasing temperature. The temperature dependence of q_c is in fact similar to that of the a component of the ICDW ordering vector in α-U [39]. Unlike α-U, there is no evidence for the wave vector being off-axis or for harmonics.

We made scans over a mesh covering $|\delta h| \leqslant 0.1$ and $|\delta k| \leqslant 0.1$ for $|\delta l| < 0.05$, about the $(1, 0, 3.5)$ reflection at 10 K (CCDW) and 60 K (ICDW). The anisotropy of the FWHM of the peak intensity is less than 2 in the h-k plane. A larger anisotropy at 60 K would be expected if the ICDW were localized at defects or surfaces confirming that the ICDW, like the CCDW, is a bulk state.

The lock-in transition coincides with a sharp peak in heat capacity at ∼46 K, shown in Fig. 6(a). The appearance of the CCDW is accompanied by an expansion of the c-lattice parameter [Fig. 5(d)] and a sharp drop of the a-lattice parameter [Fig. 5(e)]. The abruptness of the change of the a-lattice parameter is suggestive of a first-order transition, but no hysteresis was found in the expansion, the heat capacity (Sec. IV C), or resistivity (Sec. IV D).

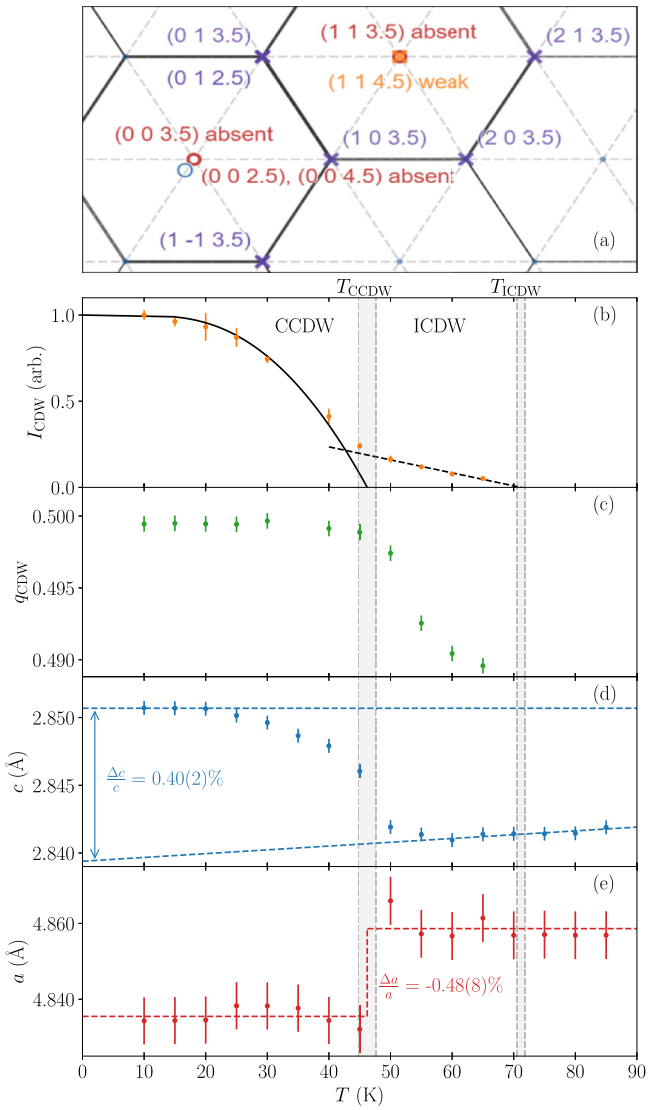

FIG. 5. (a) An overview of (h, k) diffraction space [blue circle by (0,0) and l orthogonal to the paper] with CDW reflections observed labeled as present (purple crosses), weak (orange cross), or absent (red open circles). (b) The temperature (T) dependence of normalized integrated intensity of Bragg peaks of the CDW, I_{CDW}. The solid line is a fit to the square of the BCS gap function below 46 K and the dashed line is a linear fit for temperatures above 46 K. (c) The temperature (T) dependence of the c^* component of the CDW wave vector, q_{CDW}. The wave vector is commensurate with a value $q_c = 0.4995 \pm 0.0005$ below T_{CCDW}. Above T_{CCDW} the wave vector becomes incommensurate decreasing by 2% between T_{CCDW} and T_{ICDW}. Over the same range the intensity of the peaks decreases linearly to zero. Panels (d) and (e) show the temperature dependence of the c-axis and a-axis lattice parameter. Clear changes occur crossing T_{CDW} but there is no perceptible change in behavior crossing T_{ICDW}. Figure 5(a) was generated under a CC-BY-SA-4.0 license using Desmos [40].

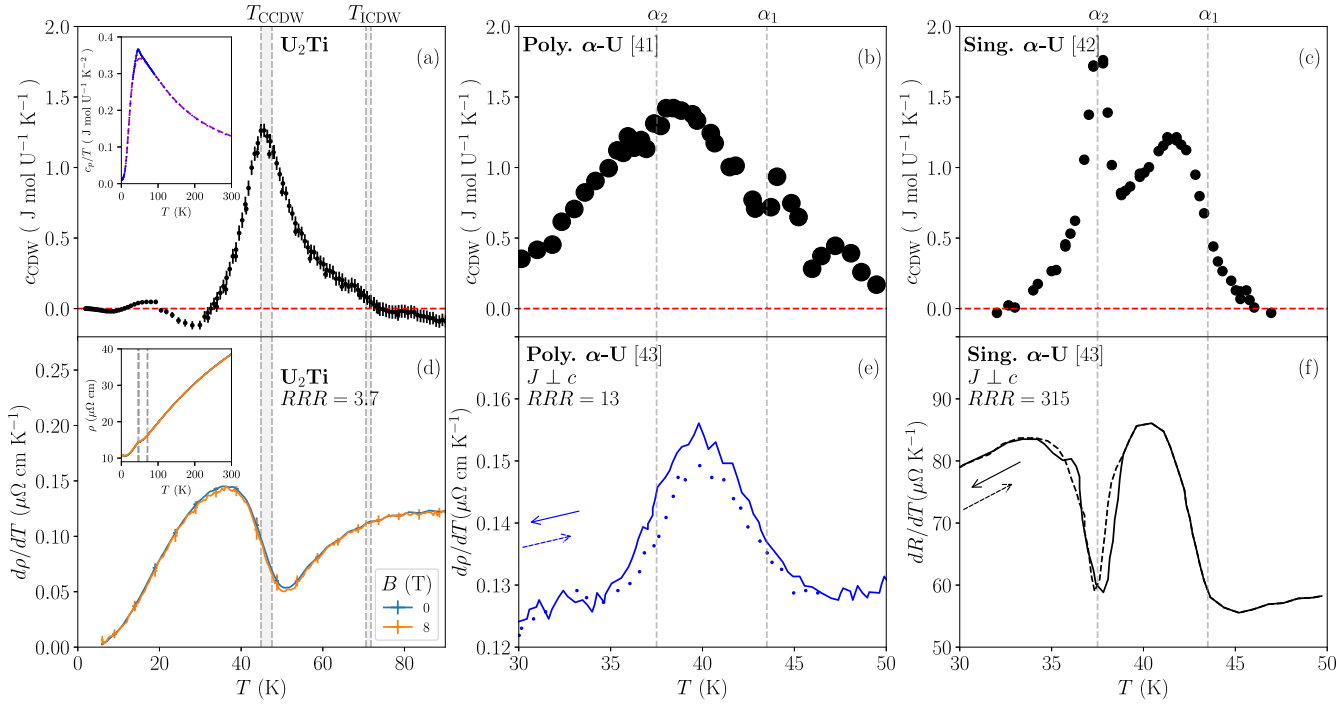

FIG. 6. (a) Inset figure shows the specific heat capacity divided by temperature, c_p/T, with a cusp anomaly at 46 K. The dashed purple line shows a fit to the background lattice and electronic heat capacity away from the CDW transitions [see main text; fit parameters $\gamma = 10.05(3)$ mJ/molU/K^2, $T_D = 154(1)$ K, $T_{E-L} = 123(1)$ K, and $T_{E-U} = 330(1)$ K]. The main figure shows the CDW heat capacity, c_{CDW}, obtained by subtracting the background contribution from the measured heat capacity. A peak in c_{CDW} occurs at T_{CCDW} with a small shoulder at T_{ICDW}. (b) and (c) Background-subtracted heat capacity in the vicinity of the α_1 and α_2 transitions for polycrystalline α-U from Crangle *et al.* [41] and single-crystal α-U from Lashley *et al.* [42]. (d) The inset figure shows the T dependence of resistivity, ρ, of a twinned sample of U_2Ti at 0 T and 8 T. The main figure shows the derivative of the resistivity, $d\rho/dT$. (e) and (f) $d\rho/dT$ of a polycrystalline α-U and temperature differential of the resistance, dR/dT, of a higher RRR single crystal, both data sets from Schmiedeshoff *et al.* [43], measured on warming (dotted curve) and cooling (solid curve).

Assuming the intensity of the satellite peaks is attributed to the displacement, δz, of U sites, the ratio of the intensity at half-integer l to integer l reflections (ignoring Debye-Waller and extinction corrections) gives $\delta z/c$ in the range 1.92%–2.16% at 10 K. The result is substantially smaller than the DFT prediction of $\delta z/c \approx 5.2\%$ [16].

C. Heat capacity

Two transitions are identified from the heat capacity. The heat capacity arising from the charge order, c_{CDW}, is calculated after the subtraction of a smooth background contribution that accounts for a conduction electron (γT) and a lattice contribution. The 3 acoustic phonon modes are modeled with a Debye contribution and 6 optic modes with two additional Einstein contributions (per U_2Ti), giving a total background contribution c_p^{back} per formula:

$$c_p^{back} = \gamma T + \tfrac{1}{3}[c_{Deb}(T, T_D) + c_{Ein}(T, T_{E-L}) + c_{Ein}(T, T_{E-U})]. \quad (2)$$

A fit to Eq. (2) for temperatures away from the CDW transitions is shown by the dashed line in the inset of Fig. 6(a). The value of γ was fixed from the low-temperature heat capacity for $T < 6$ K by fitting to $c_p/T = \gamma + \beta T^2$. The other parameters in Eq. (2) are chosen to describe c_p for temperatures $|T - T_{CCDW}| > 1.5\Gamma$. Γ is the full width at half maximum of a Lorentzian fit to the excess heat capacity above c_p^{back} centered at $T_{CCDW} \sim 46$ K. The value of Γ was determined self-consistently to be $\Gamma = (12.3 \pm 0.5)$ K. Changing the temperature range over which the CDW contribution is considered to be significant, e.g., from $\pm 1.5\Gamma$ to $\pm 2\Gamma$ about T_{CCDW}, does not significantly change the estimate of c_{CDW}.

The Sommerfeld coefficient $\gamma \sim (10.05 \pm 0.03)$ mJ mol U^{-1} K^{-2}, which is comparable to (10.0 ± 0.4) mJ mol U^{-1} K^{-2} for α-U [41]. The value of γ is higher than 7.38 mJ mol U^{-1} K^{-2} predicted in the DFT calculations for the undistorted δ structure. Kaur *et al.* predict a 15% increase of the density of states (DOS) in the distorted δ_2 state [16] but the value from our measurements exceeds this. The enhancement relative to the DFT prediction is modest compared with heavy-fermion materials, but may nevertheless represent the presence of correlations not captured by DFT.

$c_{CDW} = c_p - c_p^{back}$ is shown in the main plot of Fig. 6(a) and reveals two main features: (i) a weak shoulder feature at T_{ICDW} and (ii) a large symmetric peak at T_{CCDW}. No hysteresis is observed between cooling and warming within the experimental error of the measurements (±0.3% of the measured value).

The disordered Peierls model [44] gives broadened second-order transitions that may provide an explanation of the form of c_{CDW} we see. This model has been applied to the CDW

transition(s) in the manganites [45] and to α-U [46], for both CCDW and ICDW transitions. The broadness of the transition is due to the correlation length divergence being restricted by impurities.

Below T_{ICDW}, c_{CDW} increases until T_{CCDW}. The dirty Peierls model gives asymmetric peaks skewed to the low-temperature side of the transitions which is hard to reconcile with our data. Instead the extra heat capacity between the transitions we see might be due to the melting of discommensurations, as discussed by McMillan in the context of the CCDW transition in the transition metal dichalcogenides [47]. However, such discommensurations would require harmonics of the observed q_{CDW} ordering vector which are not seen in our XRD study of the incommensurate phase.

The much stronger heat capacity signature and coupling to the lattice parameters at the lower transition suggests that the change occurring across T_{CCDW} is more substantial than just a small change in the CDW modulation vector, for example due to the onset of a second order parameter describing the displacement of the crystalline lattice. X-ray diffraction directly probes the electron density. The modulation of the nuclear density could be probed with neutron scattering. It would be interesting to track the relative magnitude of these two modulations with temperature across the different phases.

For α-U the CDW wave vector below α_1 is incommensurate, with its major component along the a direction. In the α_2 state this component locks in to a value of 0.5, similar to the behavior of U_2Ti. It is therefore interesting to compare the form of c_{CDW} for U_2Ti with that measured for both pseudosingle crystals [42] and polycrystals of α-U [41]. The single crystals show a sharp peak of $C(T)$ at T_{CCDW} and a broadened second-order-like jump at T_{ICDW}. Both transitions were interpreted to be first order. In lower-quality polycrystals the peak at T_{CCDW} and jump are both broadened resulting in a single broad peak centered just above T_{CCDW} with a shoulder at T_{ICDW}. The data for U_2Ti appear to be intermediate between these two cases, but with the step at T_{ICDW} weaker relative to the peak at T_{CCDW}.

The peak of c_{CDW} for U_2Ti at T_{ICDW} is unlike the heat capacity of $Er_5Ir_4Si_{10}$ [15]. For $Er_5Ir_4Si_{10}$, the entropy change (of $\sim 0.3R$) occurs predominately at the upper incommensurate transition, with no significant feature at the lower commensurate transition. However, as the incommensurate phase is accompanied by a commensurate structural distortion, it is difficult to separate the commensurate/incommensurate contributions in a clean way.

D. Resistivity

The Fig. 6(d) inset shows the resistivity, ρ, of U_2Ti, and the main figure shows the derivative of the resistivity, $d\rho/dT$, versus temperature at applied magnetic fields of 0 T and 8 T. For comparison (e) and (f) show the temperature derivative of the resistance of polycrystalline and single-crystal samples of α-U (the data shown are for samples 5 and 2 in [43]).

For U_2Ti from 80–150 K $d\rho/dT$ is weakly temperature dependant compared with the vicinity of the CDW transitions, with ρ having a Bloch-Grüneissen form for isotropic phonon scattering [48]. The weak negative curvature at higher temperature may be to the resistivity approaching a saturation value. The Mott-Ioffe-Regel limit for the saturation of the resistivity is estimated from the electron density and lattice parameters to be $\rho_{\mathrm{MIR}} \sim 160\ \mu\Omega$ cm [49]. Below 80 K $d\rho/dT$ falls suggesting $\rho \rightarrow$ constant with a large residual resistivity. This could be due to impurity-like scattering from the ICDW. Below T_{CCDW}, commensuration of the CDW removes the effective disorder, and $d\rho/dT$ rises and $\rho(T)$ crosses over to a metallic-like behavior with a lower residual resistivity.

In the vicinity of a magnetic critical point the temperature derivative of the magnetic contribution to resistivity often has the same critical behavior as the magnetic specific heat [50]. This is due to the contribution from short-range spin fluctuations. The similarity of these quantities is clear for the itinerant long-wavelength incommensurate helimagnet MnSi [51]. This motivates comparison of the $d\rho/dT$ to the specific heat for CDW ordering, although charge fluctuations are different from magnetic fluctuations. For α-U, $d\rho/dT$ has a more complex structure than c_{CDW}. A connection can however be made if the peak at T_{CCDW} "contributes" to $d\rho/dT$ with an opposite sign to the jump in $C(T)$ at T_{ICDW}. For U_2Ti any link between $d\rho/dT$ and $C(T)$ appears more tenuous. With decreasing temperature the drop of $d\rho/dT$ below T_{ICDW} and rise at T_{CDW} are more easily understood in terms of disorder scattering from the ICDW state as described earlier.

The change in resistance between 0 and 8 T for U_2Ti over the full temperature range 2–300 K is $<1.2\%$. $d\rho/dT$ in the vicinity of the CDW transitions does not vary detectably with magnetic field confirming that the transitions are nonmagnetic. This corresponds to the DFT calculations with $U < 1$ eV.

α-U shows a variation in the differential of the resistivity with respect to field at the commensuration CDW transitions [43] which led to suggestions of a mixed SDW/CDW state, despite the low anisotropy of the magnetoresistance. This might explain the stronger link between $d\rho/dT$ and $C(T)$ in α-U compared to U_2Ti. The magnetic field independence of $d\rho/dT$ for U_2Ti suggests U_2Ti hosts a pure CDW state.

E. Hall coefficient

The Hall coefficient, R_H, is shown in Fig. 7 for an applied field of 8 T. No hysteresis in the Hall signal is observed between increasing or decreasing temperature.

Since U_2Ti is a compensated metal, the mobilities of the charge carriers will be important in determining the temperature dependence of the Hall coefficient at all magnetic fields.

A relative change in mobility of different bands with temperature unrelated to any CDW could give a similar behavior to that observed, as seen for example in elemental Ti [52]. While changes of Fermi surface topology related to the CDW would also modify ρ_{Hall}, ρ_{Hall} could be dominated by the evolution of unreconstructed regions of the Fermi surface.

For α-U, ρ_{Hall} shows a broad drop with decreasing temperature which sharpens and strengthens in higher-quality samples to become a more steplike change with a change of sign, occurring at the final commensurate α_3 transition [43,52].

ρ_{Hall} for U_2Ti looks similar to the result for lower-quality α-U. Changes in ρ_{Hall} with decreasing temperature onset at

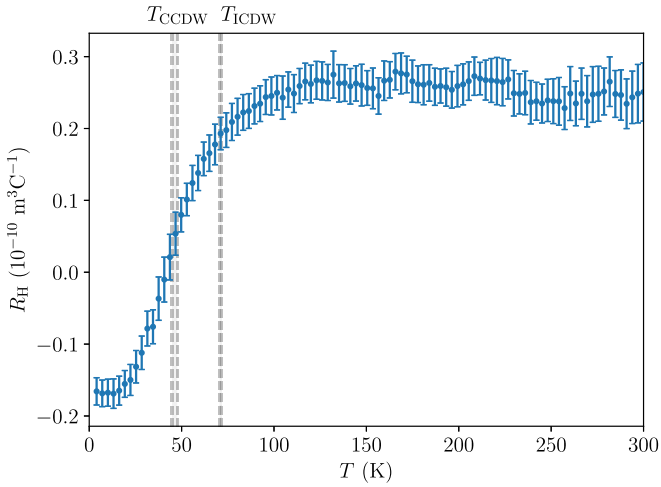

FIG. 7. The Hall coefficient, R_H, plotted versus temperature, T, determined with applied fields of ±8 T. The sign change in the Hall coefficient about T_{CCDW} could demonstrate that the transition involves some change in the dominate carrier type.

temperatures slightly higher than the value of T_{ICDW} identified by XRD. This is similar to the onset of the drop in $d\rho/dT$. However, unlike for $d\rho/dT$ no additional feature is resolved crossing T_{CCDW}. This might be taken to indicate that there is no abrupt change in electronic structure at T_{CCDW} with changes in scattering crossing T_{CCDW} affecting all bands equally. We are unable to quantify how much of the broader drop in ρ_{Hall} is directly due to the onset of CDW order or is due more simply to a background evolution of the mobility in unreconstructed regions of the Fermi surface. Unlike the case of α-U we find no evidence for any magnetic field dependence of the Hall signal.

V. CONCLUSIONS

We have discovered the existence of an incommensurate CDW (ICDW) transition at 71(1) K in twinned samples of hexagonal U_2Ti. For temperature below 46(3) K, there is a lock-in transition to a commensurate CDW (CCDW). The CCDW is consistent with a Peierls-like distortion of U positions along the crystallographic c axis predicted by Kaur *et al.* [16].

Our DFT calculation of the Lindhard function shows the dominant contribution at q_{CDW} arises from interband transitions between the two bands with largest Fermi surface area. Both planar parts and tubes making up these surfaces contribute. The calculation gives the ordering vector to be at the BZ edge ($q_c = 0.500 \pm 0.005$) with a sharp peak along c at this wave vector. It should be noted that the DFT for the state with the doubled unit cell is stable with positive phonon energies, confirming the DFT predicted ordering vector, independently of any approximations in neglecting the matrix elements in calculating the electrical susceptibility.

It is then surprising that the order at T_{ICDW} is at a slightly different vector ($q_c = 0.4896 \pm 0.0005$). The origin of this difference requires explanation. Approaches to understanding this go beyond standard DFT.

The CDW transitions in U_2Ti are shown to be similar to the α_1 and α_2 transitions of α-U, but q_{CDW} is simpler without components along different crystallographic directions. Differences are however apparent in the relative weights of the thermodynamic and transport signatures accompanying the first appearance of the ICDW and lock-in transitions.

For U_2Ti, there are rapid changes in the lattice parameters only at the lock-in transition, suggesting this transition is strongly coupled to the lattice but that the ICDW is not. The onset of the ICDW has no clear signatures in the resistivity and only gives a weak shoulder in the heat capacity. The Hall coefficient shows large changes beginning just above T_{ICDW}, with no feature at the lock-in transition, although the Hall signal may be unrelated to the CDW. The above observations all contrast with α-U, where strong features in $c_p(T)$, ρ, and $d\rho/dT$ occur at the onset of the ICDW as well as at T_{CCDW}. For high-RRR samples the Hall effect for α-U only shows a clear change at the lowest temperature lock-in transition α_3. Some of these differences in transport may stem from a coupling between spin and charge densities in α-U that is completely absent in U_2Ti.

The resulting lack of strong features in the resistivity and heat capacity motivates the reinvestigation of many U-dense materials by diffraction measurements to look for reflections associated with the formation of ICDW states. The ICDW transitions of α-U are unique among 3D materials, but perhaps a wider family of this type remains to be identified.

ACKNOWLEDGMENT

We acknowledge support from the UK EPSRC Grant No. EP/R013004/1.

[1] R. Arpaia, S. Caprara, R. Fumagalli, G. De Vecchi, Y. Y. Peng, E. Andersson, D. Betto, G. M. De Luca, N. B. Brookes, F. Lombardi, M. Salluzzo, L. Braicovich, C. Di Castro, M. Grilli, and G. Ghiringhelli, Dynamical charge density fluctuations pervading the phase diagram of a Cu-based high-T_c superconductor, Science **365**, 906 (2019).

[2] G. Seibold, R. Arpaia, Y. Y. Peng, R. Fumagalli, L. Braicovich, C. Di Castro, M. Grilli, G. C. Ghiringhelli, and S. Caprara, Strange metal behaviour from charge density fluctuations in cuprates, Commun. Phys. **4**, 7 (2021).

[3] H. Kobayashi, Y. Sakaguchi, H. Kitagawa, M. Oura, S. Ikeda, K. Kuga, S. Suzuki, S. Nakatsuji, R. Masuda, Y. Kobayashi, M. Seto, Y. Yoda, K. Tamasaku, Y. Komijani, P. Chandra, and P. Coleman, Observation of a critical charge mode in a strange metal, Science **379**, 908 (2023).

[4] C. D. O'Neill, J. L. Schmehr, and A. D. Huxley, Multicomponent odd-parity superconductivity in UAu_2 at high pressure, Proc. Natl. Acad. Sci. USA **119**, e2210235119 (2022).

[5] M. Ichimura, M. Fujita, and K. Nakao, Charge-density wave with imperfect nesting and superconductivity, Phys. Rev. B **41**, 6387 (1990).

[6] T. Kiss, T. Yokoya, A. Chainani, S. Shin, T. Hanaguri, M. Nohara, and H. Takagi, Charge-order-maximized momentum-dependent superconductivity, Nat. Phys. **3**, 720 (2007).

[7] D. Jérome, Organic conductors: From charge density wave TTF-TCNQ to superconducting $(TMTSF)_2PF_6$, Chem. Rev. **104**, 5565 (2004).

[8] A. Sanna, C. Pellegrini, E. Liebhaber, K. Rossnagel, K. J. Franke, and E. K. U. Gross, Real-space anisotropy of the superconducting gap in the charge-density wave material $2H$-$NbSe_2$, npj Quantum Mater. **7**, 6 (2022).

[9] X. Teng, J. S. Oh, H. Tan, L. Chen, J. Huang, B. Gao, J.-X. Yin, J.-H. Chu, M. Hashimoto, D. Lu, C. Jozwiak, A. Bostwick, E. Rotenberg, G. E. Granroth, B. Yan, R. J. Birgeneau, P. Dai, and M. Yi, Magnetism and charge density wave order in kagome FeGe, Nat. Phys. **19**, 814 (2023).

[10] G. H. Lander, E. S. Fisher, and S. D. Bader, The solid-state properties of uranium: A historical perspective and review, Adv. Phys. **43**, 1 (1994).

[11] J. C. Marmeggi, G. H. Lander, and T. Brückel, Progress towards producing a monodomain in the charge-density-wave state of alpha-uranium, Solid State Commun. **87**, 837 (1993).

[12] T. Gruner, D. Jang, Z. Huesges, R. Cardoso-Gil, G. H. Fecher, M. M. Koza, O. Stockert, A. P. Mackenzie, M. Brando, and C. Geibel, Charge density wave quantum critical point with strong enhancement of superconductivity, Nat. Phys. **13**, 967 (2017).

[13] H. D. Yang, P. Klavins, and R. N. Shelton, Low-temperature physical properties of $R_5Ir_4Si_{10}$ (R = Dy, Ho, Er, Tm, and Yb) compounds, Phys. Rev. B **43**, 7688 (1991).

[14] H. Cao, B. C. Chakoumakos, X. Chen, J. Yan, M. A. McGuire, H. Yang, R. Custelcean, H. Zhou, D. J. Singh, and D. Mandrus, Origin of the phase transition in $IrTe_2$: Structural modulation and local bonding instability, Phys. Rev. B **88**, 115122 (2013).

[15] F. Galli, S. Ramakrishnan, T. Taniguchi, G. J. Nieuwenhuys, J. A. Mydosh, S. Geupel, J. Lüdecke, and S. van Smaalen, Charge-density-wave transitions in the local-moment magnet $Er_5Ir_4Si_{10}$, Phys. Rev. Lett. **85**, 158 (2000).

[16] G. Kaur, S. M. Jaya, and B. K. Panigrahi, Phonon instability and charge density wave in U_2Ti, J. Alloys Compd. **730**, 36 (2018).

[17] M. D. Johannes and I. I. Mazin, Fermi surface nesting and the origin of charge density waves in metals, Phys. Rev. B **77**, 165135 (2008).

[18] S. Raymond, J. Bouchet, G. H. Lander, M. Le Tacon, G. Garbarino, M. Hoesch, J.-P. Rueff, M. Krisch, J. C. Lashley, R. K. Schulze, and R. C. Albers, Understanding the complex phase diagram of uranium: The role of electron-phonon coupling, Phys. Rev. Lett. **107**, 136401 (2011).

[19] A. P. Roy, N. Bajaj, R. Mittal, P. D. Babu, and D. Bansal, Quasi-one-dimensional Fermi surface nesting and hidden nesting enable multiple Kohn anomalies in α-uranium, Phys. Rev. Lett. **126**, 096401 (2021).

[20] A. W. Overhauser, Spin density waves in an electron gas, Phys. Rev. **128**, 1437 (1962).

[21] A. W. Overhauser and G. Lacueva, Theory of the fourfold induced-torque anisotropy in potassium, Phys. Rev. B **66**, 165115 (2002).

[22] G. Lacueva and A. W. Overhauser, Quantum oscillations from the cylindrical Fermi-surface sheet of potassium created by the charge-density wave, Phys. Rev. B **46**, 1273 (1992).

[23] L. Fast, O. Eriksson, B. Johansson, J. M. Wills, G. Straub, H. Roeder, and L. Nordström, Theoretical aspects of the charge density wave in uranium, Phys. Rev. Lett. **81**, 2978 (1998).

[24] P. Toledano and J.-C. Toledano, *Landau Theory of Phase Transitions: Application to Structural, Incommensurate, Magnetic and Liquid Crystal Systems*, Vol. 3 (World Scientific, Singapore, 1987).

[25] U. Karahasanovic, F. Krüger, and A. G. Green, Quantum order-by-disorder driven phase reconstruction in the vicinity of ferromagnetic quantum critical points, Phys. Rev. B **85**, 165111 (2012).

[26] G. Abdul-Jabbar, D. A. Sokolov, C. D. O'Neill, C. Stock, D. Wermeille, F. Demmel, F. Krüger, A. G. Green, F. Lévy-Bertrand, B. Grenier, and A. D. Huxley, Modulated magnetism in PrPtAl, Nat. Phys. **11**, 321 (2015).

[27] O. Bikondoa, L. Bouchenoire, S. D. Brown, P. B. J. Thompson, D. Wermeille, C. A. Lucas, M. J. Cooper, and T. P. A. Hase, XMaS @ the ESRF, Philos. Trans. R. Soc. A **377**, 20180237 (2019).

[28] *Physical Property Measurement System: Heat Capacity Option User's Manual* (Quantum Design Inc., San Diego, CA, 2004).

[29] B. L. Brandt, D. W. Liu, and L. G. Rubin, Low temperature thermometry in high magnetic fields. VII. Cernox™ sensors to 32 T, Rev. Sci. Instrum. **70**, 104 (1999).

[30] G. Kresse and J. Furthmüller, Efficient iterative schemes for *ab initio* total-energy calculations using a plane-wave basis set, Phys. Rev. B **54**, 11169 (1996).

[31] J. P. Perdew, K. Burke, and M. Ernzerhof, Generalized gradient approximation made simple, Phys. Rev. Lett. **77**, 3865 (1996).

[32] A. Togo, F. Oba, and I. Tanaka, First-principles calculations of the ferroelastic transition between rutile-type and $CaCl_2$-type SiO_2 at high pressures, Phys. Rev. B **78**, 134106 (2008).

[33] S. L. Dudarev, G. A. Botton, S. Y. Savrasov, C. J. Humphreys, and A. P. Sutton, Electron-energy-loss spectra and the structural stability of nickel oxide: An LSDA+U study, Phys. Rev. B **57**, 1505 (1998).

[34] A. Georges, G. Kotliar, W. Krauth, and M. J. Rozenberg, Dynamical mean-field theory of strongly correlated fermion systems and the limit of infinite dimensions, Rev. Mod. Phys. **68**, 13 (1996).

[35] B. Amadon, First-principles DFT+DMFT calculations of structural properties of actinides: Role of Hund's exchange, spin-orbit coupling, and crystal structure, Phys. Rev. B **94**, 115148 (2016).

[36] L. Miao, S. Liu, Y. Xu, E. C. Kotta, C.-J. Kang, S. Ran, J. Paglione, G. Kotliar, N. P. Butch, J. D. Denlinger, and L. A. Wray, Low energy band structure and symmetries of UTe_2 from angle-resolved photoemission spectroscopy, Phys. Rev. Lett. **124**, 076401 (2020).

[37] A. G. Knapton, The crystal structure of TiU_2, Acta Crystallogr. **7**, 457 (1954).

[38] J. L. Murray, Ti-U (titanium-uranium), in *Binary Alloy Phase Diagrams* (ASM International, The Netherlands, 1995).

[39] G. Grübel, J. D. Axe, D. Gibbs, G. H. Lander, J. C. Marmeggi, and T. Brückel, Incommensurate charge-density-wave state in α-uranium: A high-resolution x-ray and neutron-scattering study, Phys. Rev. B **43**, 8803 (1991).

[40] https://www.desmos.com/

[41] J. Crangle and J. Temporal, Heat capacity and transformations in α uranium at low temperature, J. Phys. F **3**, 1097 (1973).

[42] J. C. Lashley, B. E. Lang, J. Boerio-Goates, B. F. Woodfield, G. M. Schmiedeshoff, E. C. Gay, C. C. McPheeters, D. J. Thoma, W. L. Hults, J. C. Cooley, R. J. Hanrahan, Jr., and J. L.

Smith, Low-temperature specific heat and critical magnetic field of α-uranium single crystals, Phys. Rev. B **63**, 224510 (2001).

[43] G. M. Schmiedeshoff, D. Dulguerova, J. Quan, S. Touton, C. H. Mielke, A. D. Christianson, A. H. Lacerda, E. Palm, S. T. Hannahs, T. Murphy, E. C. Gay, C. C. McPheeters, D. J. Thoma, W. L. Hults, J. C. Cooley, A. M. Kelly, R. J. Hanrahan, Jr., and J. L. Smith, Magnetotransport and superconductivity of α-uranium, Philos. Mag. **84**, 2001 (2004).

[44] P. Chandra, Fluctuation effects on the Pauli susceptibility at a Peierls transition, J. Phys.: Condens. Matter **1**, 10067 (1989).

[45] S. Cox, J. C. Lashley, E. Rosten, J. Singleton, A. J. Williams, and P. B. Littlewood, Evidence for the charge-density-wave nature of the stripe phase in manganites, J. Phys.: Condens. Matter **19**, 192201 (2007).

[46] S. Cox, E. Rosten, R. D. McDonald, and J. Singleton, Comment on "pinning frequencies of the collective modes in α-uranium", Phys. Rev. Lett. **98**, 249701 (2007).

[47] W. L. McMillan, Theory of discommensurations and the commensurate-incommensurate charge-density-wave phase transition, Phys. Rev. B **14**, 1496 (1976).

[48] P. Allen, Boltzmann theory and resistivity of metals, in *Quantum Theory of Real Materials* (Kluwer, Boston, 1996).

[49] M. Gurvitch, Ioffe-Regel criterion and resistivity of metals, Phys. Rev. B **24**, 7404 (1981).

[50] M. E. Fisher and J. S. Langer, Resistive anomalies at magnetic critical points, Phys. Rev. Lett. **20**, 665 (1968).

[51] S. M. Stishov, A. E. Petrova, S. Khasanov, G. K. Panova, A. A. Shikov, J. C. Lashley, D. Wu, and T. A. Lograsso, Heat capacity and thermal expansion of the itinerant helimagnet MnSi, J. Phys.: Condens. Matter **20**, 235222 (2008).

[52] T. G. Berlincourt, Hall effect, resistivity, and magnetoresistivity of Th, U, Zr, Ti, and Nb, Phys. Rev. **114**, 969 (1959).